Bioactive Materials 17 (2022) 379–393

Contents lists available at ScienceDirect

Bioactive Materials

journal homepage: www.keaipublishing.com/en/journals/bioactive-materials

Osteoporotic bone recovery by a bamboo-structured bioceramic with controlled release of hydroxyapatite nanoparticles

Rui Zhao, Tieliang Shang, Bo Yuan, Xiangdong Zhu, Xingdong Zhang, Xiao Yang *

National Engineering Research Center for Biomaterials, Sichuan University, Chengdu, 610064, China

ARTICLE INFO

Keywords:
Nano hydroxyapatite
Bioceramics
Osteogenesis
Bone regeneration
Osteoporosis

ABSTRACT

While most bone defects can be repaired spontaneously, the healing process can be complicated due to insufficient bone regeneration when osteoporosis occurs. Synthetic materials that intrinsically stimulate bone formation without inclusion of exogenous cells or growth factors represent a highly desirable alternative to current grafting strategies for the management of osteoporotic defects. Herein, we developed a series of hydroxyapatite bioceramics composed of a microwhiskered scaffold (wHA) reinforced with multiple layers of releasable hydroxyapatite nanoparticles (nHA). These novel bioceramics (nwHA) are tunable to optimize the loading amount of nHA for osteoporotic bone formation. The utility of nwHA bioceramics for the proliferation or differentiation of osteoporotic osteoblasts in vitro is demonstrated. A much more compelling response is seen when bioceramics are implanted in critical-sized femur defects in osteoporotic rats, as nwHA bioceramics promote significantly higher bone regeneration and delay adjacent bone loss. Moreover, the nwHA bioceramics loaded with a moderate amount of nHA can induce new bone formation with a higher degree of ossification and homogenization. Two types of osteogenesis inside the nwHA bioceramic pores were discovered for the first time, depending on the direction of growth of the new bone. The current study recommends that these tailored hybrid micro/nanostructured bioceramics represent promising candidates for osteoporotic bone repair.

1. Introduction

Osteoporosis is a skeletal disorder characterized by widespread bone disease, the incidence of which is rapidly growing as the population ages [1,2]. The loss of bone tissue, deterioration in bone quality and disruption of bone microarchitecture induce compromised bone strength and an increase in the risk of fractures. Currently, it has been estimated that more than 200 million people suffer from osteoporosis [3,4]. According to recent statistics from the International Osteoporosis Foundation, worldwide, 1 in 3 women over the age of 50 years and 1 in 5 men will experience osteoporotic fractures in their lifetime. The current clinical treatments for osteoporotic fracture are limited to a combination of aggressive surgical, implanted device, and long-term systemic drug regimens [5]. However, antiosteoporosis drug treatment can lead to long-term disadvantages, such as atypical femoral fracture, renal impairment and immune dysfunction [6,7]. To date, autogenous bone grafts are still regarded as the gold standard for bone replacement, but have limited availability and bone mass in the donor [8,9]. Further complications are a paucity of bone, decreased osteoblastic function and decreased angiogenic capacity under osteoporotic conditions, which lead to delayed-union or nonunion [10]. Thus, continuous innovations and the development of osteoporotic implants with potent osteointegration ability are needed to address unmet clinical needs.

There is growing evidence that the surface structure of bone implants has an important role in tissue regeneration [11,12]. The hierarchical hybrid micro/nanostructure has recently attracted significant attention to provide transformation “highways” on various scales and enhance innate regeneration of the human body [13]. This is indicated by the fact that this unique hierarchical structure can stimulate cellular infiltration, nutrient/waste transportation, bone ingrowth, and vascularization, even without the addition of drugs or growth factors [14,15]. Recently, Wu et al. developed a method to create micro/nanostructured surfaces on polyetherketoneketone (PEKK) composites using femtosecond lasers [16]. This surface modification technique significantly enhanced the in vivo osseointegration and long-term stability of the implant. In an in vitro study, Jiang et al. also reported that an octacalcium phosphate-modified titanium surface with a micro/nanostructure had superior chemical stability, biomineralization, and osteoblast activities

Peer review under responsibility of KeAi Communications Co., Ltd.
* Corresponding author.
E-mail address: xiaoyang114@scu.edu.cn (X. Yang).

https://doi.org/10.1016/j.bioactmat.2022.01.007
Received 28 November 2021; Received in revised form 30 December 2021; Accepted 4 January 2022
Available online 21 January 2022
2452-199X/© 2022 The Authors. Publishing services by Elsevier B.V. on behalf of KeAi Communications Co. Ltd. This is an open access article under the CC BY-NC-ND license (http://creativecommons.org/licenses/by-nc-nd/4.0/).

[17]. Moreover, in recent years, Jiang Chang's research group conducted a series of studies to demonstrate that hydroxyapatite (HA) bioceramics with a micro/nanostructure could promote both osteogenesis and angiogenesis in vivo via osteoimmunomodulation cascades [18–20]. These studies are of substantial clinical value since HA bioceramics are one of the most commonly used biodegradable bone grafting materials adopted for a variety of orthopaedic applications. Previously, our group fabricated a mechanically enhanced HA bioceramic with a microwhisker structure [21,22]. An in vivo segmental bone defect model of beagle dogs implanted with whiskered bioceramics showed high toughness and fast osseointegration. However, to overcome severe bone loss, an advanced strategy for osteoporotic bone regenerating bioceramics requires a more bioactive component than just a favourable structure.

As the main inorganic mineral constituent of bone and teeth, hydroxyapatite nanoparticles (nHA) play an essential role in hard tissue engineering because of their superior bioactivity [23]. Synthetic nHA is now used extensively in the form of components or implant coatings to improve skeletal regeneration. The biological effect of nHA has been reported to be related to its concentration and the cell type that interacts with it. In the last decade, nHA was found to be capable of inhibiting proliferation and inducing apoptosis in various cancer cells, including osteosarcoma cells, breast cancer cells, gastric cancer cells, and melanoma, but also promoting the proliferation and mineralization of osteoblastic cell lines [24–26]. Our group first discovered that low-crystallinity nHA with a size of 40–60 nm could promote the bone-forming ability of diseased osteoblasts isolated from osteoporotic bone explants [27]. We demonstrated that the effect of different concentrations of nHA on osteoblasts could be associated with gene-level regulation of sarcoplasmic/endoplasmic reticulum calcium ATPase2 (ATP2A2) and fibroblast growth factor 23 (FGF23) [21,27]. Later, we applied this nHA coating onto bioinert polyetherketoneketone (PEKK) and titanium scaffolds via sequential vacuum dipping and low-temperature sintering [26,28]. Our in vivo findings implied that the concentration of nHA released from the scaffold might play an important role in osteointegration under severe osteoporotic conditions.

In this study, we developed a series of HA bioceramics composed of a microwhiskered scaffold reinforced with multiple layers of releasable nHA. The aim of this study was to exploit this micro/nanostructure to facilely tune the amount of loaded nHA to optimize conditions for osteoporotic bone integration in vivo. Initially, we characterized the pore structure, chemical composition, and amount of the released nHA in terms of calcium ion (Ca^{2+}) concentration. We also investigated different nHA-releasing bioceramics for their effects on cell proliferation, cell area and the expression of two key genes, ATP2A2 and FGF23, in osteoporotic osteoblasts. Finally, we demonstrated that optimal micro/nanostructured HA bioceramics can serve as ideal implant materials in vivo for osteoporotic bone defect repair.

2. Materials and methods

2.1. Study design

The aim of this study was to develop a biomimetic nwHA bioceramics composed of a microwhiskered scaffold reinforced with multiple layers of releasable nHA for osteoporotic bone defect applications. Surface topography, chemical phase composition, porous structure and degradation in vitro were characterized. Osteoporotic osteoblast was used as in vitro cell models to investigate the biocompatibility and osteogenic ability of the nwHA bioceramics. The nwHA bioceramics were implanted in an osteoporotic rat bone defect model to study in vivo regeneration of osteoporotic bone defects. The changes in body weight, the motor function and serum bone turnover markers were first monitored during implantation. New bone regeneration inside and adjacent to the bioceramics were then assessed by microcomputed tomography (micro-CT) scanning and haematoxylin and eosin (H&E) staining. Subsequently, immunohistochemical staining (IHC) was conducted to explore the potential osteogenic mechanism of the nwHA bioceramics. Nanoindentation tests were performed to evaluate degree of implant osseointegration and new bone strength. Furthermore, sequential fluorescent labeling was carried out to label the mineralized tissue and reveal the time course of new bone formation and mineralization in the porous scaffolds. The number of materials and animals for each group was determined with statistically significance.

2.2. Fabrication of the wHA bioceramics

Two litres of 0.85 mol/l $Ca(NO_3)_2$ (Sigma–Aldrich, China) solution was added to 2 l of 0.55 mol/l $(NH_4)_2HPO_4$ (Sigma–Aldrich, China) solution. The mixture was then stirred for 4 h at 40 °C, wherein the pH was adjusted to 8.0 with ammonia. After maturation for 24 h, the slurry was washed with distilled water, dried at 60 °C for 24 h. The porous structure was achieved by foaming the slurry with H_2O_2 and then sintering at 1100 °C for 2 h. Briefly, 200 g of slurry, 15 ml of polyvinyl alcohol, 15 ml of cellulose, 50 ml of H_2O_2 and 120 ml of deionized water were mixed. The mixture was heated for 2 min in a microwave to generate gas and then molded in a wooden mold to obtain the porous bioceramics green body. Afterward, the green body was dried at 80 °C for 12 h and sintered at a heating rate of 5 °C min^{-1} for 6 h until 1100 °C was reached. After heating, the bioceramics were placed in the furnace until room temperature was reached. The obtained bioceramics were further modified in an aqueous system containing 1 mol/l nitric acid and deionized water (pH 4.0) and heated hydrothermally at 180 °C for 12 h. After washing and drying, the wHA bioceramics were obtained.

2.3. Preparation of nHA

One litre of 0.12 mol/l $(NH_4)_2HPO_4$ solution was added to an equal volume of 0.20 mol/l $Ca(NO_3)_2{\cdot}4H_2O$ (Sigma–Aldrich, China) solution, in which the pH was adjusted to 10 by adding ammonia. After thorough stirring for 4 h, the slurry was transferred to an autoclave for hydrothermal treatment and kept at 150 °C for 14 h. After the autoclave was cooled to room temperature naturally, the slurry was washed with distilled water 3 times.

2.4. Preparation of the nwHA bioceramics

The nwHA bioceramics were obtained by vacuum infusion of the wHA bioceramics impregnated with different concentrations of the nHA slurry. Briefly, the prepared nHA slurry was sonicated for 45 min in an ultrasonic cleaner (KQ–600KDE, China) at 100 W. Premade porous wHA bioceramics were soaked in the nHA slurry, kept under vacuum at 10 Pa for 5 min, and then sintered at 120 °C for 2 h. The above process was repeated several times to ensure that the surface of the porous bodies was fully covered by nHA. Different amounts of nHA on the scaffolds could be modulated by altering the concentration of the nHA slurry and the number of ultrasonic vacuum infusions.

2.5. Characterization of bioceramics

The X-ray diffraction (XRD, Empyrean PANalytical) with CuKα radiation at a current of 20 mA and voltage of 30 kV was used to determine the composition of the samples. The surface morphology of the implants was visualized using by scanning electron microscopy (SEM, Hitachi S4800, Japan; accelerating voltage, 20 kV). The synthetic and released nHA were examined using transmission electron microscopy (TEM, FEI, Holland). The scaffolds underwent micro-CT scanning (Scanco Medical, VivaCT 80, Switzerland) with 70 kV voltage, 114 μA current, and voxel of 10 μm. Scanco software was used to perform three-dimensional reconstruction of the obtained multi-layer scan data, and simultaneously to measure and analyse the structural parameters of the scaffolds such as porosity, mean pore diameter and pore wall thickness. The

dissolution rate of the scaffolds was tested by measuring the concentration of Ca^{2+} in a Tris buffer, as previously described [21,31]. Briefly, each bioceramic (Φ3 mm, 4 mm) was separately soaked in 1 M sterile Tris buffer at a fixed ratio of scaffold to buffer at 1 g:100 ml, and kept in sealed containers and maintained at 37 °C. At 1, 2, 3, 7, and 14 days, 500 μl aliquot of the solutions were taken out for analysis and equal fresh buffer was added to keep the constant volume. Ca^{2+} concentration was measured using with an inductively coupled plasma optical emission spectrometer (ICP-OES). According to the different concentration of Ca^{2+} released in the first three days, four nwHA bioceramics were selected for the follow-up experiments.

2.6. Cell proliferation and adhesion on scaffolds

Primary osteoblasts were derived from ovariectomized rats using our previously established method [27]. The cells were cultured in a complete medium consisting of a mixture of α-minimum essential medium (α–MEM, Gibco, USA), 10% standard fetal bovine serum (FBS, Gibco, USA) and 1% penicillin/streptomycin (Gibco, USA). The cells were seeded onto the bioceramics (2×10^5 cells/well) in 24-well plates coated with Ultra Low Attachment Surface (Corning Inc., Corning, NY). The proliferation was measured using CCK-8 (Dojindo, Kumamoto-ken, Japan). After 1, 3, and 5 days, the medium was replaced with 10% CCK-8 solution and incubated for 4 h at 37 °C. The absorbance of the formazan-dissolved solution was observed by a spectrometer at a wavelength of 450 nm. Fluorescein diacetate (FDA, Sigma–Aldrich, USA) and propidium iodide (PI, Sigma-Aldrich, USA) staining were utilized to visualize the viability of osteoblasts on different scaffolds. The samples cultured for 5 days were fixed with 4% paraformaldehyde, and labeled by incubating with Phalloidin-TRITC (Sigma) for 40 min. After rinsing with PBS (pH 7.4), the cell nuclei was contrast-labeled in blue by 4', 6-Diamidino-2-phenylin dole dihydrochloride (DAPI, Sigma). The actin cytoskeletons of cells were detected by confocal laser scanning microscopy (CLSM, TCS SP5, Leica, Germany) and the cell areas were measured by ImageJ analysis software (version 1.421).

2.7. qRT–PCR verification

The expressions of ATP2A2 and FGF23 was quantitatively analysed by qRT–PCR. The extracted RNA samples were reverse transcribed into complementary DNA (cDNA) with the iScript™ cDNA Synthesis kit (Bio–Rad, USA), and this reaction was performed using the CFX96t real-time PCR detection system (CFX960, Bio–Rad, USA) with SsoFastTM EvaGreen® Supermix (Bio–Rad, USA). Each sample was analysed in triplicates and repeated for three independent assays. The relative fold changes were calculated using the comparative quantity △△Ct method. GAPDH was chosen as the housekeeping gene to normalize the expression levels of the target genes.

2.8. Western blotting

The total protein was isolated from cells using protein lysis buffer. The protein concentration in each lysate was measured using a BCA protein assay kit (Pierce, USA). Samples were heated with boiling water for 10 min in sample buffer (Bio–Rad, USA). Equal aliquots of protein (15 mg) were separated by 10% SDS-polyacrylamide gel electrophoresis (Invitrogen, USA) and then transferred to polyvinylidene difluoride (PVDF) membranes (Bio–Rad, USA). The membrane was blocked with 1% bovine serum albumin (BSA) in 1 × TBS–T (tris-buffered saline with Tween 20), followed by incubation with primary antibodies against ATP2A2 (Cell Signaling, USA) and FGF23 (Santa Cruz, USA). The membranes were then incubated with a horseradish peroxidase–conjugated secondary antibody (Santa Cruz, USA). The protein bands were visualized by a ChemiDoc XRS + Imaging System and quantitated using Image Lab Software version 6.0 (Bio-Rad Laboratories).

2.9. Surgical procedure

All animal studies were performed in accordance with procedures approved by the Institutional Animal Care and Use Committee of Sichuan University. 12-week-old female Sprague-Dawley rats were anesthetized with 2% pentobarbital sodium (2 mg/100 g body weight) and subjected to a standard bilateral ovariectomy as previously described [21,28]. For bone implantation, the hind legs were shaved and disinfected, and the distal femur was exposed through sharp dissection. The holes were then drilled using slow drill speeds. Thirty animals were randomly divided into five groups according to implant materials. Each animal was intramuscularly injected with tetracycline (30 mg/kg; Sigma–Aldrich) 14 days before euthanasia and calcein (8 mg/kg; Sigma–Aldrich) 3 days before euthanasia (at 8 weeks after implantation). Then, animals were euthanized by 6% pentobarbital sodium (6 mg/100 g body weight) via intravenous injection. The femurs were harvested and fixed in 4% paraformaldehyde for 7 days for subsequent analyses.

2.10. Functional assessment

The motor function recovery of all animals was monitored before implantation and 1 and 7 weeks after surgery. Briefly, the rats (n = 6/group) with red ink on their hind paws were placed on a runway consisting of a white paper surface and a plastic wall. The animals were trained to make consecutive runs over the runway without any hesitation before the tests. The first 60 cm of footprints were not included in the statistics. Stride length referred to the mean distance of forward movement between each stride, while base length referred to the mean distance between the left and right hind paws.

2.11. Bone turnover markers analysis

At week 8 post-implantation, blood collected from the heart of the animals was allowed to stand for 30 min at room temperature and then centrifuged for 15 min (4000 rpm at 4 °C). The serum levels of type I collagen (CTX-1) and procollagen type I N-terminal propeptide (PINP) was quantitatively assessed using a commercial rat CTX-1 ELISA (enzyme-linked immunosorbent assay) kit (Cloud-Clone Corp., USA) and rat PINP ELISA kit (Cloud-Clone Corp., USA), respectively. All assays were performed in accordance with the manufacturer's protocol and the concentrations of CTX-1 and PINP of each sample were determined from the standard curve.

2.12. Micro-CT examination

The femurs underwent micro-CT scanning with 70 kV voltage, 114 μA current, and voxel of 10 μm. All data were analysed and 3D-reconstructed by Scanco software. During the reconstruction, the newly formed bone was segmented using a fixed global threshold. A $1 \times 1 \times 2$ mm^3 region surrounding the defect was designated the volume of interest (VOI) to study the effect of the bioceramics on adjacent bone loss. The trabecular microarchitecture parameters of the VOI were assessed. The finite element analysis (FEA) models (element size of 10 μm) of the VOI were created using a direct conversion of bone voxels to cubic hexahedral elements. The models were then imported into ANSYS Workbench (ANSYS, Canonsburg, PA) for further analysis. Material properties were applied using typical values for bone (Young's modulus of 15 GPa and Poisson's ratio of 0.3). The boundary conditions that represented uniaxial compression tests were defined to determine the bone mechanical performance.

2.13. Histological evaluation

After micro-CT examination, half of the bone samples around the implantation site were dehydrated in ascending concentrations of alcohol from 70 to 100% and then embedded in polymethyl

methacrylate. The transverse sections for each embedded sample were cut into ~100-μm-thick slices using a microtome (SAT-001, AoLiJing, China), and then ground and polished to a final thickness of 25 μm. H&E staining was then performed on the sections to quantitatively measure the relative bone area. Subsequently, CLSM was used to observe fluorescent labelling of the unstained sections with chelating fluorochromes employing excitation/emission wavelengths of 405/580 nm for tetracycline (yellow) and 488/517 nm for calcein (green). MAR was defined as the mean distance between two fluorescent labels divided by 10 days (the time interval between the two injections of fluorochrome). After CLSM detection, the sections were coated with gold and then observed using SEM-EDS to study the elemental distribution at the implant-bone interface.

2.14. Nanoindentation test

The PMMA-embedded bone samples were subjected to nanoindentation tests at room temperature using the Ultra Nano Hardness Tester (Anton Paar GmbH, Austria) with a diamond Berkovich indenter. The system was calibrated with a fused silica standard before evaluation. On the basis of optical microscopic visualization, nanoindentation points were placed at random locations inside either the remaining materials or the newly formed bone. The boundaries between new bone and the remaining material were obvious. The new bone was darker and mainly striped, while the remaining material was brighter and in granular shape. During the experiments, the applied load force and resulting depth of penetration into the samples were continuously monitored with high precision. The maximum load during indentation was 10 mN, with loading and unloading rates of 20 mN/min. Six indents were produced on each sample (n = 6/group), and these data were presented as force-displacement curves. The Oliver and Pharr's method was used to calculate the elastic modulus and hardness of the specimens. Bone was assumed to be isotropic, with a 0.3 Poisson ratio.

2.15. Immunohistochemical studies

The remaining half of the femur samples were preserved in 70% ethanol, decalcified with 10% EDTA (pH 7.4), dehydrated in a graded series of ethanol solutions and embedded in paraffin. Then, 5-μm sections were cut from the samples. Sections were processed with either H&E or immunohistochemistry staining using primary antibodies against ATP2A2 and FGF23 (1:500, Affinity Biosciences). After rinsing, the sections were incubated for 30 min with secondary antibodies and then avidin-biotin enzyme reagents, followed by counterstaining with haematoxylin. Brown staining around the tissue was observed to indicate the positive expression of ATP2A2 or FGF23 under a light microscope (BX60, Olympus, USA). Mean optical density (MOD) of the proteins was measured by ImageJ software (version 1.421).

2.16. Statistical analysis

The results are expressed as mean ± SD. Statistical analysis was performed with SPSS v19 software. Differences were evaluated using unpaired two-tailed Student's t-test for two-group comparisons and with one-way analysis of variance (ANOVA) followed by Tukey's post-hoc test for multiple group comparisons. In all the statistical evaluations, $p < 0.05$ was considered as statistically significant. All results were reproduced in at least three independent experiments.

3. Results

3.1. Fabrication of nHA releasable microwhiskered bioceramics

The enhancing effect of nHA on osteogenesis has been widely reported and TEM images of nHA can be found in Fig. S1. However, tuning the amount of nHA released is still challenging. We fabricated a series of multiple nHA layer-loaded whiskered hydroxyapatite (nwHA) bioceramics in three stages: i) modifying HA bioceramics with hydrothermal treatment to obtain a micro whiskered-structure (wHA); ii) grafting gradient concentrations of nHA slurry into the whiskered HA bioceramics via vacuum infusion; and iii) immobilizing the nHA particles entrapped in the whisker network structure with low-temperature sintering.

In stage (i), we developed a method to induce the in situ formation of bioceramic whiskers on a traditional HA surface (Fig. 1A). At the beginning of the hydrothermal reaction, bud-like nucleation sites were formed on the surface of the crystal grains. The nucleation sites were then developed into whiskers and evenly aligned on the surface. After 6 h, the number of whiskers no longer increased, but the shape of each crystal whisker changed over time. According to our previous studies, the diameter and length of whiskers can be modulated by adjusting the original phase composition of calcium phosphate bioceramics and hydrothermal parameters [29,30]. The interlacing crystal whiskers enable sufficient space for the loading of nanoparticles and appropriate compressive strength for stability at the initial stage of implantation.

In stage (ii), different nwHA bioceramics were obtained with gradient loading of nHA (Fig. 1B). The nanoparticles were initially deposited on top of the whiskers and formed a layer. The subsequent vacuum infusion process drove the nHA to penetrate into the space of the wHA network. With increasing nanoparticle concentration in the slurry and increasing infusion times, more nHA was loaded onto the bioceramic. When the concentration of the nHA slurry was higher than 70 mg/ml and the infusion time was more than 3, the interconnected pores of the bioceramic were clotted, and the interconnectivity was lost (Fig. S2). To examine the relative amount of nHA released from the nwHA surface and to determine the representative loading dosage of nHA, the Ca^{2+} concentration of the medium in the first three days was measured. The initial concentration of nHA (≤60 mg/ml) and the infusion times (≤3) were directly proportional to the concentration of Ca^{2+} released from the nwHA bioceramics (Fig. 1C). Based on the averaged results and standard deviation of 10 parallel samples per group, four nwHA bioceramics with gradient Ca^{2+} release fabricated through different nHA infusion concentrations and times were selected for further experiments.

In stage (iii), when nanoparticles were dispersed homogeneously throughout the whisker network, low-temperature sintering was performed to immobilize nHA. Based on previous experiments, we chose 120 °C as the sintering temperature because it would weakly bond nHA to the wHA bioceramics and at the same time allow the release of nHA under physiological conditions [21,22]. When the sintering temperature was above 120 °C, it resulted in the growth of HA crystals to merge nHA with each other and with the wHA bioceramics, which prevented the release of nHA to the medium.

3.2. Characterization of nwHA bioceramics

Our nwHA bioceramics were originally inspired by bamboo groves (Fig. 2A). Similar to photosynthetic bamboo leaves, the top nHA layer imparts osteogenic functions to the bioceramic scaffold, and the lower wHA whisker network provides structural toughness similar to bamboo poles. The conformational similarity of both was observed by SEM (Fig. 2B), confirming that the whisker structure of nwHA1 to nwHA4 was homogeneously covered by different amounts of nHA. The gradient release of nHA particles from the nwHA scaffold with high dispersivity, such as bamboo shed leaves, can be visualized by TEM (Fig. 2B). The degraded particles were rod-shaped with a length of approximately 50 nm. Our preliminary implantation experiment confirmed that this specific layer of nHA can effectively promote BMP-2 protein secretion and new bone formation (Fig. S3). New bone was primarily grown upon the nHA layer and formed a circle inside the pores of bioceramics.

The XRD patterns indicated that the synthesized wHA, nHA and nwHA were all composed of pure HA phase, matching well with the

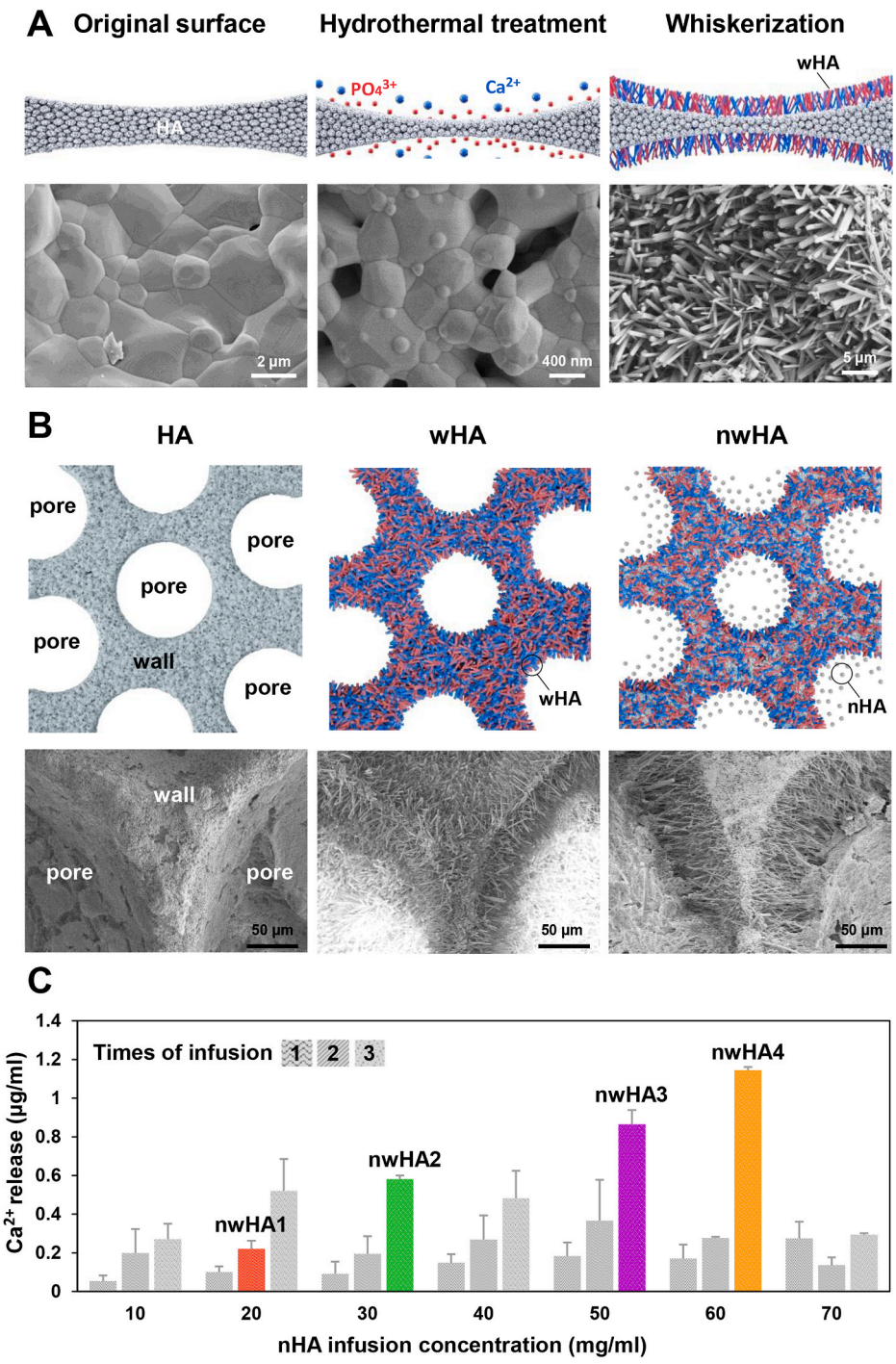

Fig. 1. Design of nano hydroxyapatite (nHA) releasable micro-whiskered bioceramics. (A) Schematic illustration of the fabrication process of micro-whiskered hydroxyapatite (wHA) bioceramics and the representative SEM images. (B) Schematic illustration of the preparation method of nHA loaded micro-whiskered hydroxyapatite (nwHA) bioceramics and the representative SEM images. (C) Ca^{2+} released profile of the nwHA bioceramics in Tris buffer (pH 7.4) in the first three days. The colored bars indicated the selected four nwHA bioceramics according to the difference in Ca^{2+} concentration. All data are reported as mean ± standard error.

standard HA diffraction pattern (09–0432, hydroxyapatite) (Fig. 2C). Microcomputed tomography imaging (micro-CT)– rendered pore structure analysis demonstrated that the nwHA1 to nwHA4 bioceramics had similar porosities (~70%) and pore diameters (~210 μm) (Fig. 2D). Due to the deposition of the nHA layer, all nwHA groups had a relatively larger pore wall thickness value than the wHA group. Again, the Ca^{2+} release level for the batch of nwHA samples used in cellular and animal experiments was characterized by days of incubation, with an order of nwHA1 < nwHA2 < nwHA3 < nwHA4 (Fig. 2D and Fig. S4).

3.3. Effects of the nwHA bioceramics on in vitro osteogenesis

We next examined the in vitro compatibility of the nwHA bioceramics with osteoblasts primarily derived from ovariectomized rats using our previously established method [21]. Osteoporotic osteoblasts spread well on all bioceramics during coculture (Fig. 3A). From Day 1 to Day 5, cells in all groups continued to proliferate, as determined by Cell Counting Kit-8 (CCK-8) assay at Days 1, 3, and 5 (Fig. 3B). More viable cells and a larger cell area were detected in the nwHA bioceramic group than in the control wHA group (Fig. 3C). As stated earlier, the expression of two key genes related to nHA-induced bone formation, ATP2A2 and FGF23, was analysed by quantitative real-time polymerase chain reaction (qRT–PCR) (Fig. 3D). The gene expression of ATP2A2 in osteoporotic osteoblasts cocultured with nwHA was significantly higher than that in osteoporotic osteoblasts cocultured with wHA, indicating a distinct effect of the nHA layer. Furthermore, nwHA2 and nwHA3 had

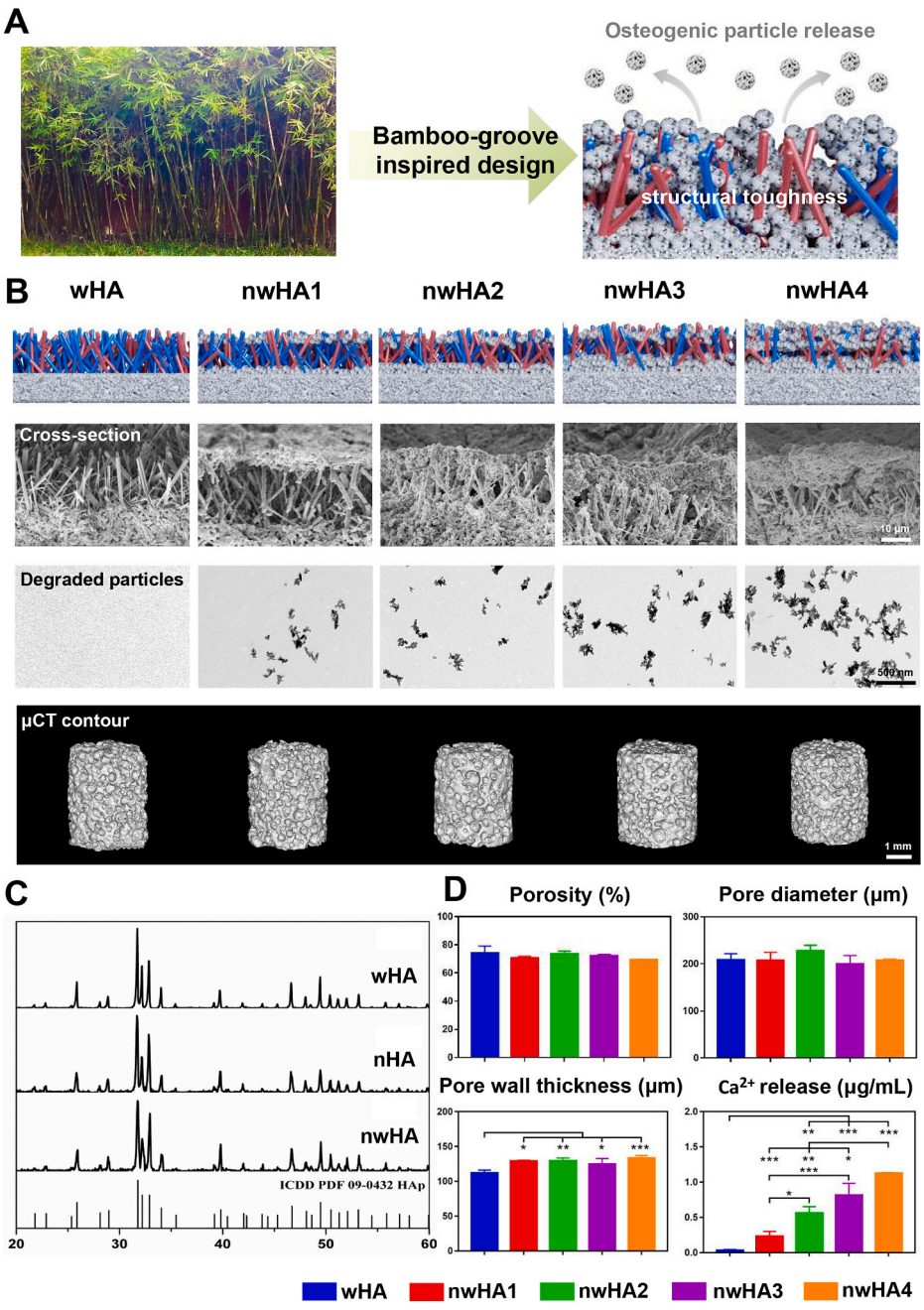

Fig. 2. Structural and compositional characterizations of the nwHA bioceramics. (A) Schematic illustration of bamboo-groove inspired design of nwHA bioceramics. (B) Schematic illustration of nwHA bioceramics with gradient nHA layers (first line) and the representative SEM (second line), TEM (third line) and micro-CT (fourth line) images of bioceramics and their degradation product. (C) XRD patterns of wHA, nHA and nwHA bioceramics. (D) Pore structure parameters rendered by micro-CT analysis and in vitro degradation profile of different nwHA bioceramics. All data are reported as mean ± standard error. ANOVA with Tukey's post hoc test $*p < 0.05$, $**p < 0.01$, $***p < 0.001$.

relatively higher ATP2A2 gene expression levels than the other two nwHA groups. For FGF23, we noticed strongly upregulated gene expression preferentially in the nwHA1 and nwHA2 groups. Western blotting analysis was generally in line with qRT–PCR results, indicating that the nwHA2 bioceramic had a superior ability to trigger an elevation in ATP2A2 and FGF23 expression, both at the gene and protein levels (Fig. 3E and Fig. S5).

3.4. Serum biomarker and animal motor function analyses

We then set out to evaluate the in vivo bone healing performance of nwHA using an osteoporotic rat model with femoral defects. We established a model with bilateral ovariectomy (OVX) and then implanted wHA, nwHA1, nwHA2, nwHA3, and nwHA4 bioceramics into the femoral metaphyseal defects of the rats 6 weeks after OVX (Fig. 4A). In vivo serum biomarker levels and animal motor function were analysed at week 8 and week 7. For serum C-terminal cross-linked telopeptides of CTX-1, a bone resorption marker, no significant difference was found among all groups (Fig. 4B). With regard to the serum PINP level, a bone formation marker, rats implanted with nwHA2 bioceramics had the highest value and stood out as the only nwHA group, demonstrating significance compared to the wHA group. Animal behaviour analysis was performed preimplantation and at week 1 and week 7 after implantation (Fig. 4C). In terms of foot placement motor function measurements, the stride length and base length of all groups dramatically decreased after bioceramic implantation due to the trauma caused by drilling during defect establishment. After 7 weeks of implant osteointegration, the base length of all groups was restored to the preimplantation level. It is worth noting that for stride length, the extent of recovery was different among groups. While the wHA group only showed an approximately 0.25 cm increase in stride length at the end of the study, the nwHA2 group presented the highest stride length recovery

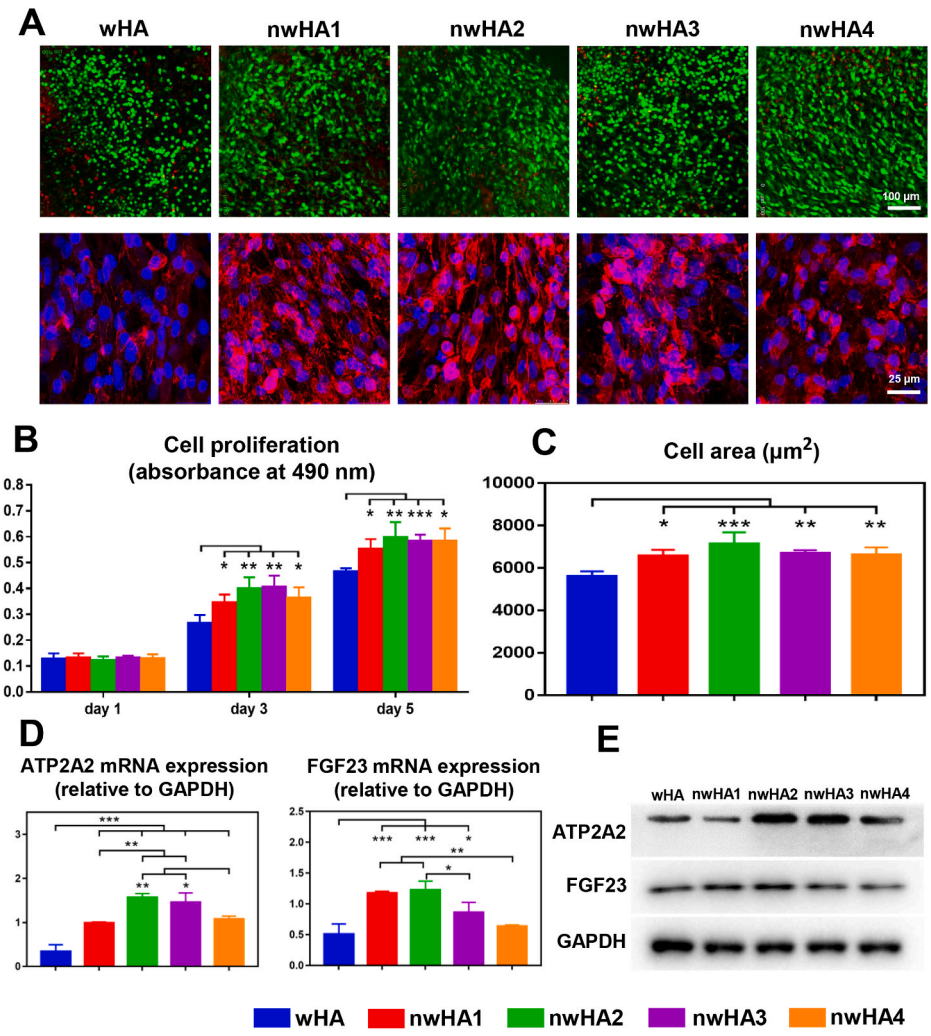

Fig. 3. Effect of nwHA bioceramics on cocultured osteoporotic osteoblasts. (A) First line: CLSM observations of live (green)/dead (red) staining of osteoporotic osteoblasts cocultured with different nwHA (first line); Second line: CLSM observations of the osteoporotic osteoblasts with F-actin stained with Phalloidin-TRITC (red) and nuclei stained with DAPI (blue). (B) Cell viability of osteoporotic osteoblasts cocultured with different nwHA bioceramics at days 1, 3, and 5. (C) Cell area quantification of osteoporotic osteoblasts from different groups on day 5. (D) qRT-PCR analysis for ATP2A2 and FGF23 gene expressions of osteoporotic osteoblasts from different groups on day 5. (E) Western blotting analysis for ATP2A2 and FGF23 protein expressions of osteoporotic osteoblasts from different groups on day 5; All data are reported as mean ± standard error. ANOVA with Tukey's post hoc test $^{*}p < 0.05$, $^{**}p < 0.01$, $^{***}p < 0.001$.

(~2 cm) at the end of the study which was comparable to that observed preimplantation.

3.5. Ingrown and adjacent bone analyses of the bioceramic implants

After implantation for 8 weeks, the bioceramic implanted bone was harvested. Gross observation indicated sufficient osteointegration of all of the implants, and no signs of infection were observed (Fig. 5A). In micro-CT reconstruction, a gap (100 μm) oriented parallel to the axis of the borehole between the implants and host bone is our region of interest to study bone integration [28,31]. Compared with the other groups, the nwHA2 and nwHA3 groups exhibited larger amounts of bone within the gap region and more new bone ingrown into the bioceramic pores. Moreover, the host trabecular bone adjacent to the implants was well maintained in the nwHA2 group, while a large hollow bone marrow region resulting from the progression of osteoporosis was observed in the other groups (Fig. 5B). Total deformation, von Mises stress and elastic strain of the trabecular bone reconstruction adjacent to the implant were visualized by FEA (Fig. 5B and Fig. S6). The nwHA2 group presented a more homogenous distribution of deformation upon loading, and no concentration of maximum deformation could be visualized.

We then quantified the above observations using micro-CT-based thresholding (Fig. 5C and Fig. S7). The amount of bone volume within the gap region was measured and normalized to the total gap volume, defined as gap bone fraction (gBV/TV). The nwHA bioceramic groups generally presented a higher gBV/TV than the wHA group. In the nwHA2 group, a prominently higher ingrown bone volume fraction (iBV/TV), adjacent bone volume fraction (aBV/TV), bone mineral density (BMD) and trabecular number (Tb.N) were observed. In contrast, other bioceramic groups showed deterioration in these parameters to various degrees due to the development of osteoporosis. We also found a lower maximum von Mises stress of the host trabecular bone around the nwHA2 implant, suggesting efficient load distribution performance. Together, these results revealed that not only was new bone formation within the bioceramic pores promoted, but adjacent bone loss due to progression of the disease was also delayed by nwHA2.

3.6. Undecalcified histological staining and mechanical behaviour of the new bone and the remaining material

Undecalcified histological examination of the implant-bone tissue sections corroborated the results obtained by micro-CT, in which more ingrown bone inside pores was observed in the nwHA2 group (Fig. 6A). The new bone formed was tightly attached to the bioceramic walls with various morphologies, which were further analysed by dynamic histomorphometry. SEM coupled with energy dispersive spectroscopy (EDS) was used to closely study the osteointegration border at the microlevel. SEM images of the unstained bone section exhibited more cracks between the wHA bioceramics and the newly formed bone, while the nwHA bioceramics were well integrated with the new bone (Fig. 6B). Quantitatively, animals implanted with nwHA2 bioceramics had the

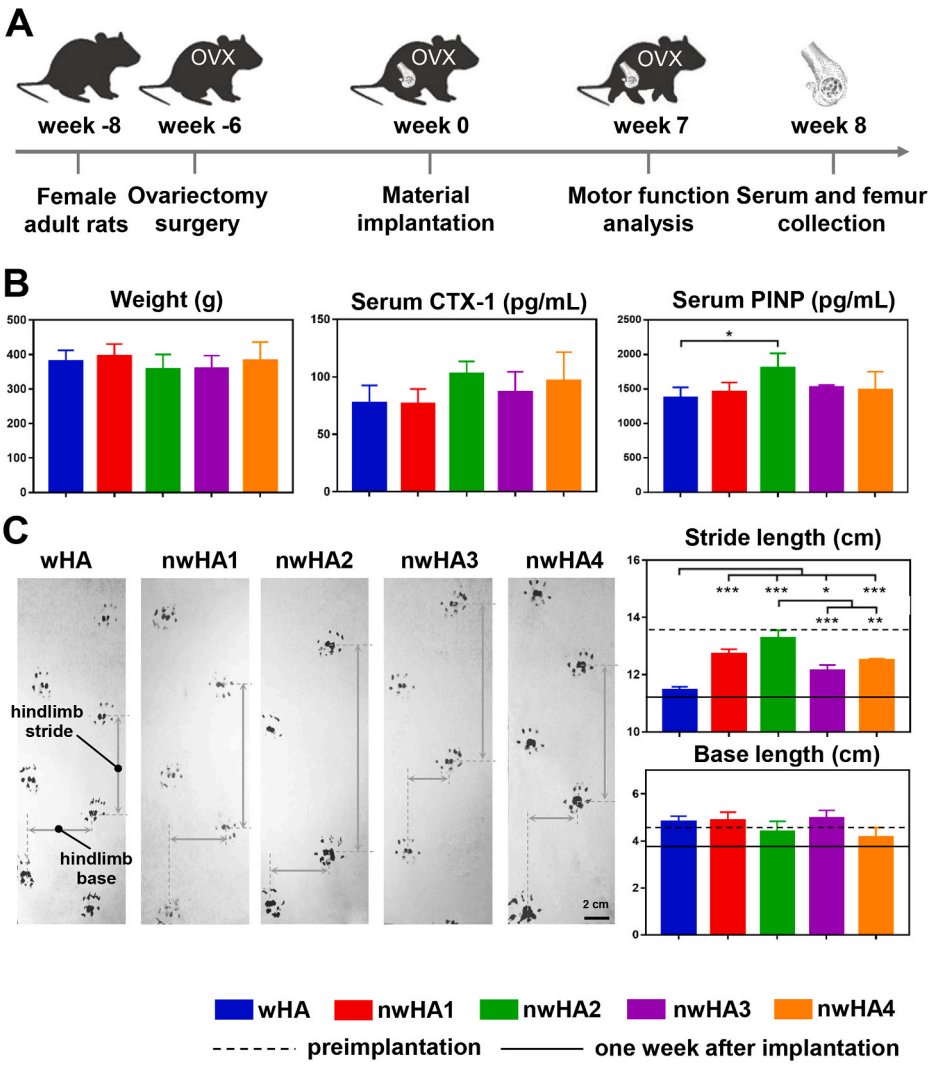

Fig. 4. In vivo evaluation of bone healing effect of the nwHA bioceramics implanted in an osteoporotic rat model with bone defect. (A) Overall timeline of the study for different experiments. (B) Animal weight change, serum levels of CTX-1 and PINP of ovariectomized rats implanted with different nwHA bioceramics at week 8 postoperatively. (C) Animal behavior analysis at week 7 postoperatively. All data are reported as mean ± standard error. ANOVA with Tukey's post hoc test $*p < 0.05$, $**p < 0.01$, $***p < 0.001$.

largest percentage of bone area, which was significantly higher than the wHA and nwHA4 groups (Fig. 6C). Furthermore, new bone integrated with nwHA2 bioceramics had a higher Ca/P molar ratio than that of the wHA group, which was the closest to the level of healthy bone (~1.67) [32]. No significant difference was found in the Ca/P molar ratio of the remaining bioceramic material among all groups.

To further assess the effect of different nHA release concentrations on the mechanical properties of the implant-bone interface, we performed nanoindentation tests on the remaining material and the adjacent new bone (Fig. 6D and E). The slope of the loading regimen of the force-indentation depth curve indicates the stiffness of the bone, which reflects the degree of mineralization [33]. Compared to all nwHA groups, we observed a lower stiffness according to the curve of the wHA group. In contrast, the stiffness of the wHA group was found to be the highest out of the remaining material among all groups, revealing an undegraded brittle bioceramic phase. Intriguingly, we observed that the nwHA2 group presented a similar force-indentation depth curve between new bone and the remaining material, revealing mechanically matched osteointegration. From the curves, the changes in the elastic modulus (b*E* and m*E*) and hardness (b*H* and m*H*) of new bone and the remaining material were determined (Fig. 6F). b*E* and b*H* of the nwHA bioceramic-implanted bone were all significantly higher than those of the wHA group. After 8 weeks of implantation, the m*E* of all bioceramic groups remained in the range of 20–40 GPa, which was significantly higher than the b*E*. Abnormally high m*H* was measured in the wHA group, which was approximately 2-fold higher than the b*H* value of this group. However, the nwHA2, nwHA3 and nwHA4 groups had similar m*H* and b*H* values, indicating a homogenous hardness distribution at the implant border.

3.7. *In vivo expression of ATP2A2 and FGF23 induced by bioceramics*

Next, we performed H&E staining and ATP2A2 and FGF23 staining to validate the corresponding in vitro osteogenesis results. In accordance with previous results, more new bone was formed in the porous structure of the nwHA2 bioceramic, while little was found in the wHA bioceramic (Fig. 7A). Furthermore, we observed more ATP2A2-and FGF23-positive staining areas in the nwHA1, nwHA2 and nwHA3 groups (Fig. 7B and 7C). The quantitative histomorphometrical analysis of osteoblast number supported the observation that bone formation was prominently elevated in the nwHA2 group compared with the other groups (Fig. 7D). ATP2A2 was deposited abundantly in the nwHA groups but not in the wHA group, with the highest ATP2A2 protein expression measured in the nwHA2 group among all groups. FGF23 protein expression shared a similar trend. These findings were consistent with the in vitro qRT–PCR and Western blotting analysis of ATP2A2 and FGF23.

Bone regeneration requires angiogenesis, which provides nutrition for new bone formation. Thus, the in vivo preliminary vascularization ability of the bioceramics was also characterized with these decalcified slices (Fig. S8). The nwHA2 and nwHA3 groups exhibited abundant

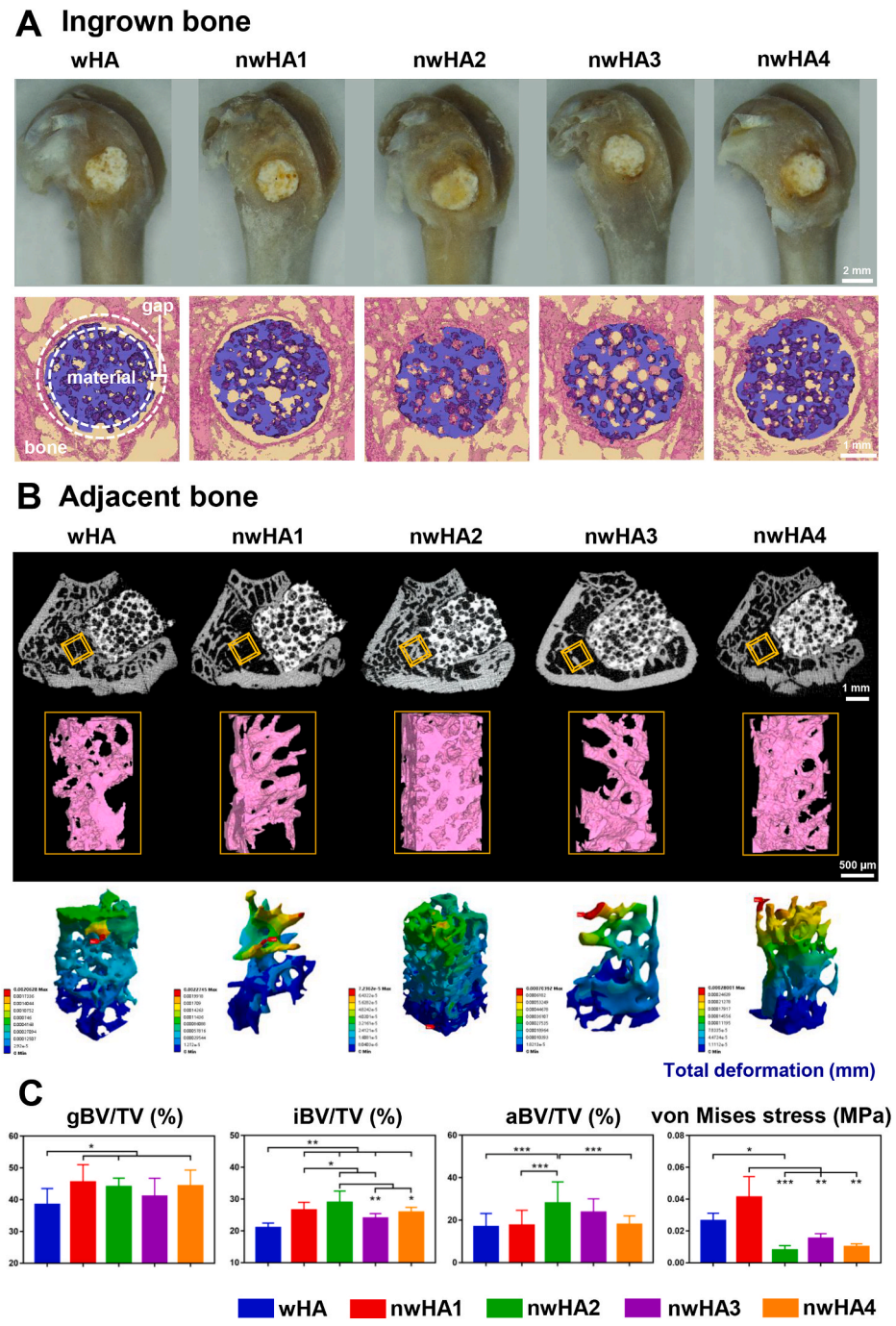

Fig. 5. Ex vivo evaluation of bone healing effect of the nwHA bioceramics implanted in an osteoporotic rat model with bone defect. (A) Gross observation and micro-CT reconstructed images of the nwHA bioceramics implanted in rat metaphyseal bone with osteoporosis. (B) First line: 2D cross-sectional X-ray images of the implant-bone interface; Second line: 3D micro-CT rendered images of the trabecular bone adjacent to the defect as the VOI; Third line: FEA predicted total deformation of the VOI under load. (C) Quantification of gap bone fraction (gBV/TV), ingrown bone volume fraction (iBV/TV), adjacent bone volume fraction (aBV/TV), and maximum von Mises stress of VOI. All data are reported as mean ± standard error. ANOVA with Tukey's post hoc test $*p < 0.05$, $**p < 0.01$, $***p < 0.001$.

vessel-like structures embedded in the new bone matrix inside the pore structure and more $CD31^{+}Emcn^{+}$ double-positive capillaries than the other groups. This recently discovered capillary type is able to link angiogenesis with subsequent osteogenesis [34,35].

3.8. Dynamic histomorphometry evaluations

In vivo sequential fluorescence labelling with tetracycline (yellow) and calcein (green) provided profound information related to new bone formation "movement" within the porous structure of the bioceramics. Dynamic histomorphometry is a traditional technique widely used to study bone development. However, it has seldom been exploited to characterize bioceramic-induced osteoconduction phenomena. Based on a large number of slices, we categorized five patterns of new bone formation on the surface of the bioceramics (Fig. 8A). New bone tissue could crawl along the pore wall, bridge two distant walls together, infiltrate and adhere down to the pore, and join two adjacent pores. At the implant-host bone interface, dynamic osteogenesis mainly presented a tendency to wrap the remaining materials (Fig. 8B). Furthermore, we discovered two types of osteogenic directions inside the pores, on which bone was deposited. One was named type I osteogenesis, that is, the direction of new bone formation was towards the wall of the adjacent pore wall. Another was named type II osteogenesis, when the direction of new bone formation was away from the adjacent pore wall. These two osteogenesis types could cooccur in a single bioceramic pore. Even though the differences did not reach statistical significance among all groups according to mineral apposition rate (MAR) analysis, it is worth noting that type I osteogenesis predominantly occurred in the nwHA2

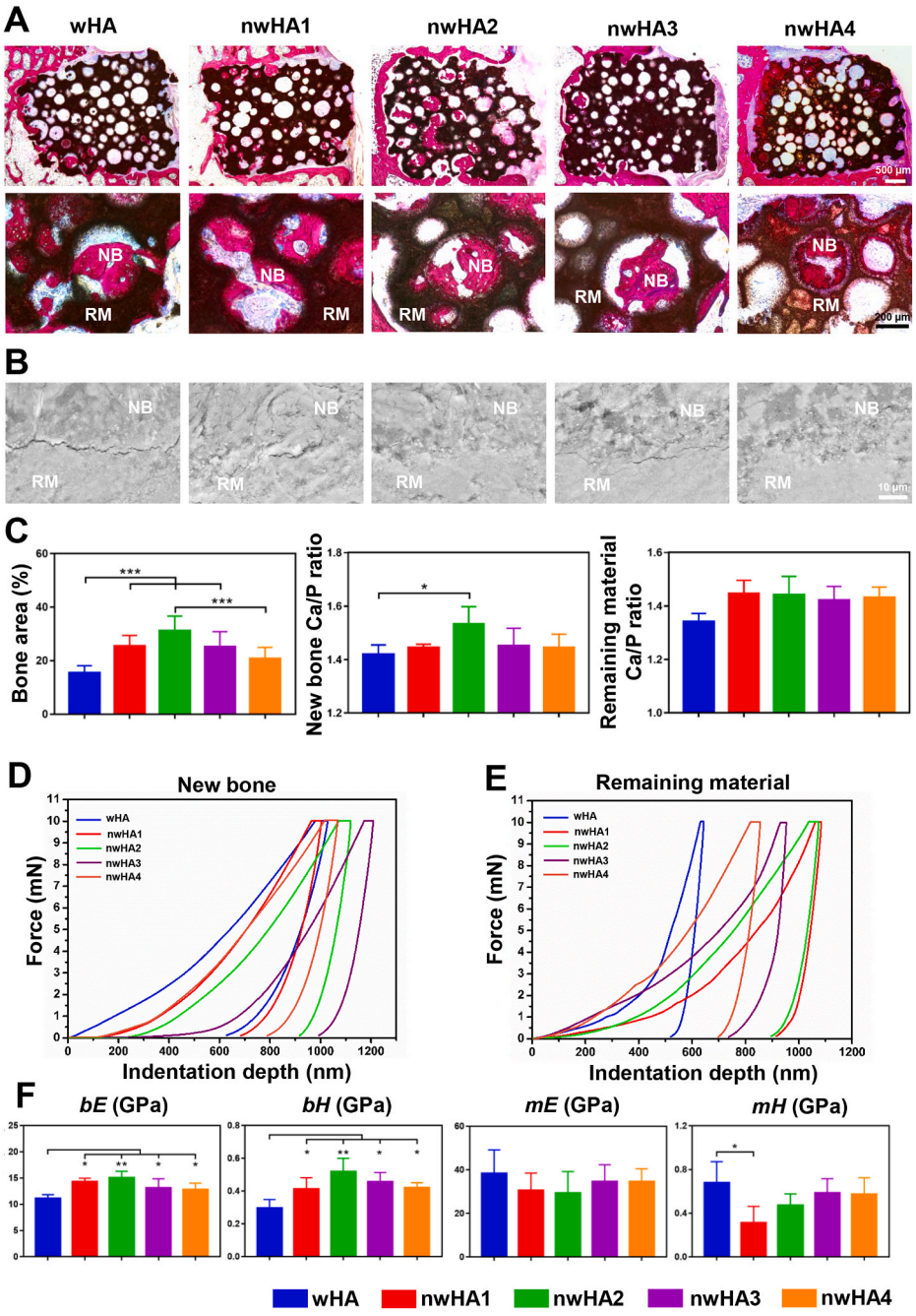

Fig. 6. Histological analysis and biomechanical test for osteoporotic bone regeneration induced by different nwHA bioceramics. (A) Undecalcified H&E staining showing position of the newly formed bone within the implanted nwHA bioceramics (NB: new bone, RM: remaining material). (B) SEM observation of the border between the new bone and the remaining material. (C) Quantification of bone area, Ca/P ratio in the new bone and remaining material detected by EDS. (d, e) Typical load-displacement curves generated from nano-indentation test on ingrown new bone and remaining material. (F) Averaged elastic modulus (b*E*) and hardness (b*H*) of the newly formed bone, and averaged elastic modulus (h*E*) and hardness (h*H*) of the undegraded material. All data are reported as mean ± standard error. ANOVA with Tukey's post hoc test $^{*}p < 0.05$, $^{**}p < 0.01$, $^{***}p < 0.001$.

group (Fig. 8C). In contrast, wHA, with the least potency in bone regeneration was the only group that showed major type II osteogenesis, indicating that the presence and amount of nHA could affect the osteogenesis direction inside the pore structure. Subsequently, we studied the correlation between pore diameter and osteogenesis type. We found that type I osteogenesis was present in bioceramic pores with a relatively larger diameter (200–300 μm) than type II osteogenesis (150–250 μm). This result suggested that the pore diameter also played a critical role in the direction of osteogenesis. Moreover, type I osteogenesis contributed more to the total MAR measured.

4. Discussion

While most bone defects can be repaired spontaneously, the healing process can be complicated due to insufficient bone regeneration when osteoporosis occurs [36]. To circumvent the side effects of anti-osteoporosis drug administration, developing tissue engineering scaffolds to affect the metabolism of local bone tissue aimed at osteogenic induction would be a good strategy. Growing evidence suggests that micro-/nanotopographical cues of scaffolds play an important role in osteoblastic cell functionality [17,37,38]. Accelerated defect healing can be achieved by tailoring the bone graft surface structure into a multiscale organization. Guided microwhisker formation is a widely used technique in electronic engineering and civil engineering, aiming to reinforce the mechanical performance of composite materials, i.e., cements or alloys. For example, Wang et al. recently demonstrated that the addition of calcium carbonate whiskers into gas storage cement would result in a 62.3% increase in tensile strength and a 47% increase in compressive strength [39]. They observed that calcium carbonate whiskers could bridge cracks, effectively prevent the development and diffusion of cracks, and eventually enhance cement deformability under loading. As shown in this study, the formation of HA microwhiskers is

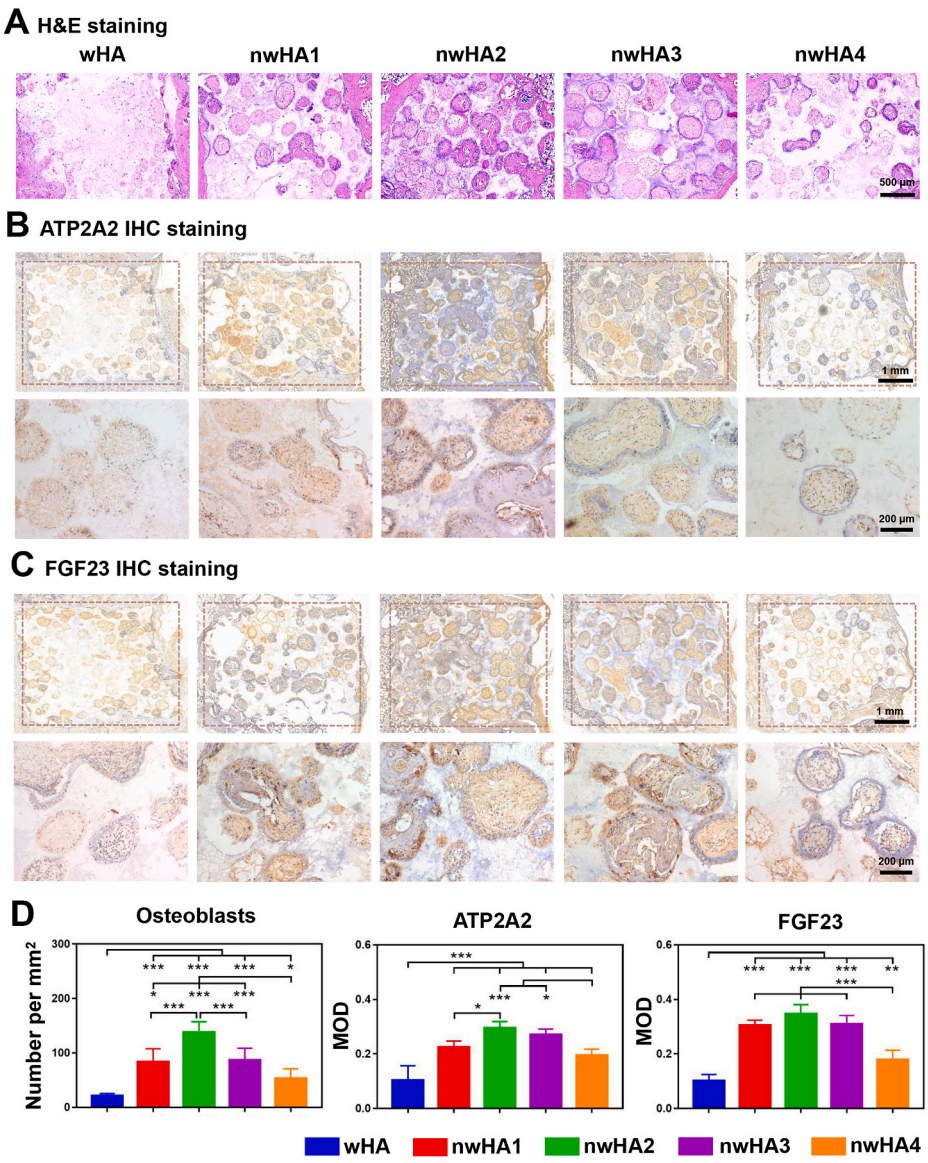

Fig. 7. Immunohistochemical analysis for osteoporotic bone regeneration induced by different nwHA bioceramics. (A) Decalcified H&E staining showing position of the newly formed bone within the implanted nwHA bioceramics. (B) ATP2A2 and (C) FGF23 staining of histological sections for different groups and the enlarged images of the pore region inside bioceramics. (D) Quantitative analysis of osteoblasts per unit area and mean fluorescence intensity values of ATP2A2 and FGF23. All data are reported as mean ± standard error. ANOVA with Tukey's post hoc test $*p < 0.05$, $**p < 0.01$, $***p < 0.001$.

comprised of a nucleation phase and growth phase, which are fundamentally stress relief phenomena [40]. When the temperature is lower than 120 °C, there is insufficient atomic diffusion to form HA microwhiskers, and when the temperature is higher than 120 °C, there is no driving force because of stress relief. Our group had previously established a hydrothermal protocol to control the length and thickness of the microwhiskers [30,41,42], which served as an excellent platform for localized nHA release in the current study. Here, we developed a strategy to deposit nHA layers into microwhiskered porous bioceramics via alternant vacuum infusion and lower-temperature sintering procedures. By adjusting the infusion times and nHA slurry concentration, a bamboo grove-like micro/nanostructured surface was built on the pore walls of HA bioceramics. The chemical composition of these nwHA bioceramics was purely hydroxyapatite, and the macroporous structure was well maintained. During in vitro degradation, these nwHA bioceramics were demonstrated to release nHA in a gradient concentration.

Our goal was to exploit this nwHA structure to tune the amount of loaded nHA to optimize the conditions for osteoporotic bone integration. nHA has been reported to promote cell adhesion and proliferation and can exert osteogenic effects on cells in vitro. It was further confirmed in the present study that when cocultured with osteoporotic osteoblasts, all nwHA bioceramic groups had a positive effect on cell proliferation and adherence, attributed to the flat surface built by nHA particles. More importantly, osteoporotic osteoblasts presented higher ATP2A2 gene and protein expression when cocultured with nwHA2, a nwHA bioceramic loaded with a moderate amount of nHA. ATP2A2 is an ATPase actively involved in intracellular Ca^{2+} uptake into the endoplasmic reticulum of osteoblasts [43]. We and others have previously shown that the expression of ATP2A2 was significantly downregulated in osteoporotic individuals compared to healthy controls [27,44]. It was first found in a quantitative proteomic analysis by Zhao et al. that nHA-loaded polyetheretherketone (PEEK) implant material induced 2.5-fold higher ATP2A2 expression in osteoblastic cells than pure PEEK material [45]. We also showed that cell culture medium containing nHA could upregulate ATP2A2 expression in osteoporotic osteoblasts; however, the positive effect was not diminished in a dose-dependent manner at higher concentration [27]. Similarly, we observed that cellular ATP2A2 expression was only increased in the bioceramic groups loaded with moderate amounts of nHA, nwHA2 and nwHA3. Moreover, the trends of gene and protein expression of FGF23, a putative marker for bone formation [46,47], were aligned with the ATP2A2 results. These in vivo findings were later confirmed by IHC staining of the implanted bioceramics, suggesting that the osteoporotic osteoblasts actively adjusted their bone forming ability only upon stimulation with a specific

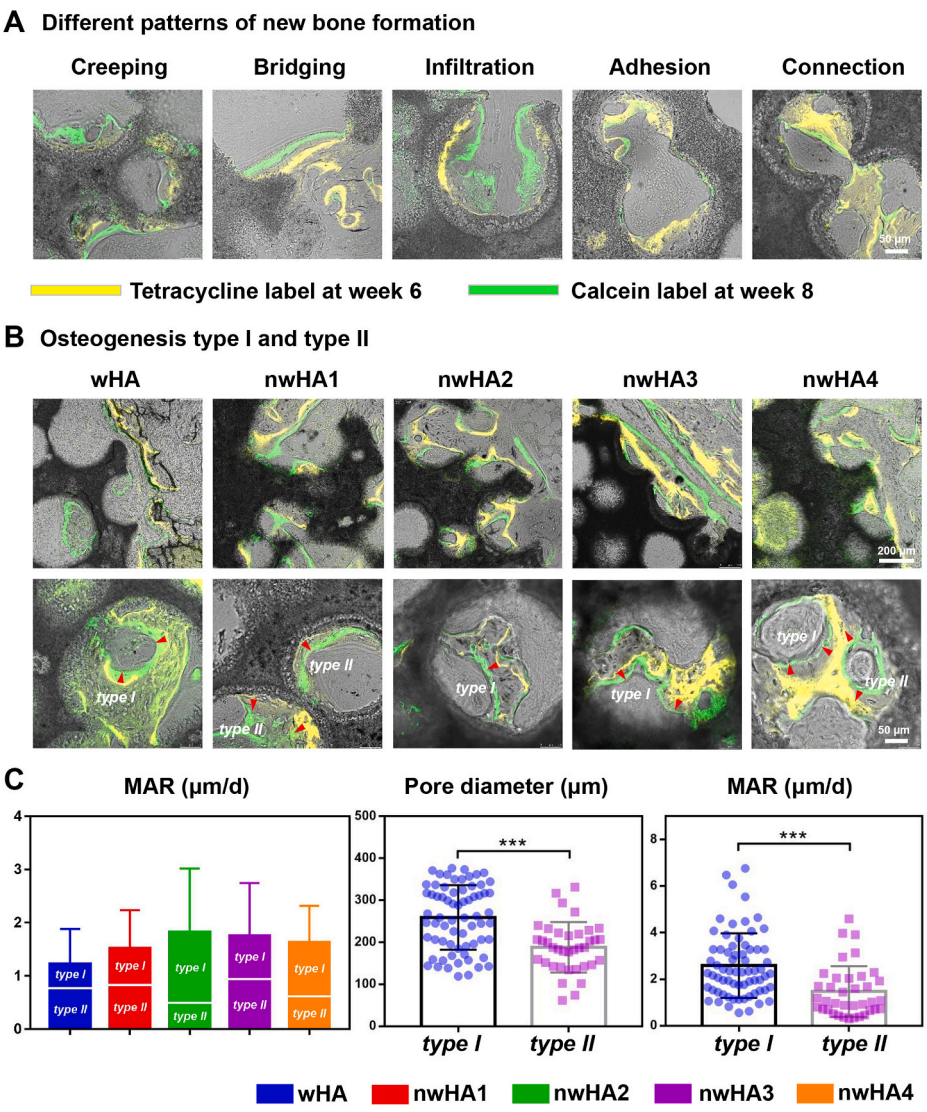

Fig. 8. In vivo sequential fluorescence labeling of new bone formation inside porous nwHA bioceramics (yellow, tetracycline label; green, calcein label). (A) Observed patterns of new bone formation. (B) Two types of osteogenesis discovered inside the pore structure of nwHA bioceramics. (C) Comparison of mineral apposition rate (MAR) between different nwHA groups; Statistical analysis of the relationship between osteogenesis type and pore diameter of the bioceramics, and the relationship between osteogenesis type and the MAR.

nHA concentration.

A primary characteristic of successful biomaterials for osteoporotic bone repair is their bone formation ability under in vivo pathological conditions. Animal motor behaviour analysis, especially foot placement, is often used to assess the overall functional recovery of animals as a noninvasive technique [48]. In an osteoporotic rat femur defect model, we observed that the stride lengths of all groups were dramatically decreased one week after implantation, indicating severely impaired motor function after bone injury [49]. After implantation for 7 weeks, rats from the nwHA2 group presented a higher stride length value restored to the preimplantation level. In addition, serum biomarker analysis showed a higher PINP level in the nwHA2 group than in the wHA group. Serum PINP is a marker of bone formation and has been widely used in both animal experiments and clinical trials to assess the therapeutic effects of antiosteoporosis drugs [50]. It was determined that to achieve fast osteointegration, implants used in osteoporotic bone repair should not only provide mechanical support in the defect but also ameliorate bone loss near the implant due to continuing osteoporosis [51,52]. While most of the previous work focused merely on implant ingrown bone formation, our current study has taken one step further by including new bone formation adjacent to the implant into consideration. First, our micro-CT analysis revealed that all nwHA bioceramics had a higher ingrown bone volume ratio than wHA, indicating that more bone was formed attaching to the pore walls with nHA releasing ability. In addition, the nwHA2 bioceramic was more advantageous in maintaining the adjacent osteoporotic bone volume, BMD, and trabecular microstructural parameters. These micro-CT-generated adjacent bone quantity data were supported by FEA analysis, which further indicated that an efficient load distribution mechanism in the nwHA2 group could be ascribed to more host trabeculae formed around the bioceramic implant. These findings suggested that the surrounding osteoporotic bone tissue could largely benefit from a certain amount of nHA release.

A thorough and complete understanding of what happens at the bone–implant interface is important to assess the extent of osteointegration. Histological staining analysis of the retrieved samples was consistent with the micro-CT results showing that the nwHA groups had more new bone formed along the interior pore walls of the bioceramics than the wHA group. Among them, the nwHA2 group had the highest bone area ratio and osteoblast numbers. We then used nanoindentation to probe new bone quality. Nanoindentation has emerged as a new tool to assess the intrinsic mechanical properties of implant-bone intermediates at high resolution of displacement and load [53,54]. It allows researchers to investigate the microlevel elasticity and hardness at any region of interest and to distinguish the remaining material from the new bone attached. Previously, we used a nanoindentation technique to measure the biomechanical property changes in PEKK and bioceramics after implantation [22,28,31], and in bones upon the application of different anti-osteoporosis drug treatments [55]. We discovered that the

average elastic modulus of the bony matrix reflected its collagen content, whilst the hardness was related to the hard mineral content. The b*E* and b*H* values of the newly formed bone adjacent to the nwHA2 bioceramics were comparable to those of the ibandronate- or PTH-treated bones. This implied that a moderate amount of nHA released from the implant might be an efficient way to increase osteoporotic bone strength at the interface, almost equivalent to the level of drug administration. Compared to wHA, a significantly higher b*H* value observed in the nwHA2 group was in accordance with a higher calcium/phosphate ratio characterized by SEM/EDS analysis, indicating a more mature bone matrix with higher mineral content [32,56]. Aligned with our previous findings, the retrieved bioceramic implants with poor osteointegration ability, such as wHA here, possessed an abnormally higher m*E* and m*H* than the host bone due to the undegraded material brittleness and phase composition [31,57]. However, bioceramic implants that could integrate well with host bone, such as nwHA2, often presented a force-indentation depth curve similar to that of newly formed bone, revealing a higher degree of ossification and homogenization [22].

An intriguing phenomenon was observed in sequential fluorescent staining of the new bone mineralization edge at a time interval of 2 weeks. First, several patterns of vigorous active osteoconduction were identified. The fabricated nwHA bioceramics were endowed with a highly osteoconductive micro/nanostructure that permits bone growth on its surface or down into pores via channels. Osteoconduction by definition is general, which means that bone grows on a surface. Here, we discovered various patterns of vivid osteoconduction in which the new bone tissue may creep along the bioceramic pore wall, bridge two distant bioceramic struts, infiltrate and attach into the pores, and connect two pores through a narrow interconnection (<50 μm). Second, and more importantly, we characterized two types of osteogenesis inside the bioceramic pores, depending on the direction of growth of new bone. In type I osteogenesis, the bone regeneration direction is towards the adjacent pore wall, and in type II osteogenesis, the bone regeneration direction is away from the adjacent pore wall. Type I and II osteogenesis were not independent and could coexist even in a single bioceramic pore. We then performed quantitative comparisons between these two types. In the nwHA2 bioceramic with potent osteogenic ability, type I osteogenesis contributed more to new bone formation, while the result in the wHA group was the opposite. Pore diameter is the main limiting factor of osteogenesis [58,59]. Among biomaterials, scaffolds with 200–300 μm pores have the best osteogenic effect when implanted [60]. Here, we observed that type I osteogenesis occurred in bioceramic pores with a relatively larger diameter (200–300 μm), and type II osteogenesis existed more in bioceramic pores with a smaller pore diameter (150–250 μm). Osteogenesis does not occur without a proper blood supply. In the current study, the nwHA2 and nwHA3 groups exhibited more $CD31^{+}Emcn^{+}$ double-positive capillaries than the other groups. This newly discovered capillary type is able to mediate perivascular osteoprogenitor differentiation and couple angiogenesis to osteogenesis [34,35]. $CD31^{+}Emcn^{+}$ double-positive capillaries were specifically embedded in the new bone matrix within the nwHA2 and nwHA3 bioceramic pores, indicating that an appropriate range of nHA loading enhanced early angiogenesis related to osteoporosis. Overall, our findings complement the current understanding of bioceramic-induced osteogenesis.

5. Conclusion

In this study, we developed a series of nwHA bioceramics composed of a microwhiskered scaffold reinforced with multiple layers of releasable nHA. Our goal was to exploit these nwHA bioceramics for application in osteoporotic bone repair. Our results showed that all nwHA bioceramics demonstrated good biocompatibility when cocultured with osteoporotic bone-derived osteoblasts. Genes involved in intracellular Ca^{2+} uptake and osteoporotic bone formation were specifically upregulated in the nwHA2 group loaded with moderate amounts of nHA. Not only was in vivo new bone formation within the porous structure promoted, but adjacent bone loss due to progression of osteoporosis was also delayed by nwHA2 bioceramics. Furthermore, the intrinsic bone mechanical quality at the microlevel was enhanced by the local release of nHA, as reflected by FEA and nanoindentation analyses. For the first time, two types of osteogenesis inside bioceramic pores were discovered, depending on the direction of growth of new bone. These novel micro/nanostructured nwHA bioceramics show good potential as bone grafts to repair osteoporotic fractures.

CRediT authorship contribution statement

Rui Zhao: Methodology, Validation, Formal analysis, Data curation, Writing – original draft. **Tieliang Shang:** Methodology, Formal analysis. **Bo Yuan:** Methodology, Data curation. **Xingdong Zhang:** Conceptualization, Resources, Conceptualization, Resources, Supervision. **Xiao Yang:** Writing – review & editing, Supervision, Resources, Funding acquisition.

Declaration of competing interest

The authors declare that they have no known competing financial interests or personal relationships that could have appeared to influence the work reported in this paper.

Acknowledgements

This project was funded by National Natural Science Foundation of China (grant no. 81971755), Sichuan Science and Technology Program (2020YFS0038) and Fundamental Research Funds for the Central Universities. We thank Dr. Li Chen from the Analytical & Testing Center of Sichuan University for assistance with micro-CT images.

Appendix A. Supplementary data

Supplementary data to this article can be found online at https://doi.org/10.1016/j.bioactmat.2022.01.007.

References

[1] I.R. Reid, A broader strategy for osteoporosis interventions, Nat. Rev. Endocrinol. 16 (6) (2020) 333–339, https://doi.org/10.1038/s41574-020-0339-7.
[2] N.R. Fuggle, E.M. Curtis, K.A. Ward, N.C. Harvey, E.M. Dennison, C. Cooper, Fracture prediction, imaging and screening in osteoporosis, Nat. Rev. Endocrinol. 15 (9) (2019) 535–547, https://doi.org/10.1038/s41574-019-0220-8.
[3] J.A. Kanis, N. Burlet, C. Cooper, P.D. Delmas, J.Y. Reginster, F. Borgstrom, European guidance for the diagnosis and management of osteoporosis in postmenopausal women, Osteoporos. Int. 30 (1) (2019) 3–44, https://doi.org/10.1007/s00198-018-4704-5.
[4] S. Tumay, O. Lale, C.B. Nursel, An overview and management of osteoporosis, Eur. J. Rheumatol. 4 (1) (2017) 46–56, https://doi.org/10.5152/eurjrheum.2016.048.
[5] E. Hsu, N. M, Advances in treatment of glucocorticoid-induced osteoporosis, Curr. Opin. Endocrinol. Diabetes Obes. 24 (6) (2017) 411–417, https://doi.org/10.1097/MED.0000000000000368.
[6] J. Schilcher, V. Koeppen, P. Aspenberg, K. Michaëlsson, Risk of atypical femoral fracture during and after bisphosphonate use, Acta Orthop. 371 (10) (2015) 100–107, https://doi.org/10.3109/17453674.2015.1004149.
[7] R. Rizzoli, J.Y. Reginster, S. Boonen, G. Bréart, A. Diez-Perez, D. Felsenberg, J. M. Kaufman, J.A. Kanis, C. Cooper, Adverse reactions and drug–drug interactions in the management of women with postmenopausal osteoporosis, Calcif. Tissue Int. 89 (2) (2011) 91–104, https://doi.org/10.1007/s00223-011-9499-8.
[8] W.G.D. Long, T.A. Einhorn, K. Koval, M. Mckee, T. Watson, Bone grafts and bone graft substitutes in orthopaedic trauma surgery, J. Bone Joint Surg. Br. 89 (3) (2007) 649–658, https://doi.org/10.2106/JBJS.F.00465.
[9] Z.S. Tao, W.S. Zhou, Z. Qiang, K.K. Tu, Z.L. Huang, H.M. Xu, T. Sun, Y.X. Lv, W. Cui, L. Yang, Intermittent administration of human parathyroid hormone (1-34) increases fixation of strontium-doped hydroxyapatite coating titanium implants via electrochemical deposition in ovariectomized rat femur, J. Biomater. Appl. 30 (7) (2016) 952–960, https://doi.org/10.1177/0885328215610898.
[10] P. Mora-Raimundo, D. Lozano, M. Manzano, M. Vallet-Regí, Nanoparticles to knockdown osteoporosis-related gene and promote osteogenic marker expression for osteoporosis treatment, ACS Nano 13 (5) (2019) 5451–5464, https://doi.org/10.1021/acsnano.9b00241.

[11] J. Guo, X. Tian, D. Xie, K. Rahn, J. Yang, Citrate-based tannin-bridged bone composites for lumbar fusion, Adv. Funct. Mater. 30 (27) (2020) 2002438, https://doi.org/10.1002/adfm.202002438.
[12] Q. Vallmajo Martin, N. Broguiere, C. Millan, M. Zenobi, M. Ehrbar, PEG/HA hybrid hydrogels for biologically and mechanically tailorable bone marrow organoids, Adv. Funct. Mater. 30 (48) (2020) 1910282, https://doi.org/10.1002/adfm.201910282.
[13] R. Chen, J. Wang, C. Liu, Biomaterials act as enhancers of growth factors in bone regeneration, Adv. Funct. Mater. 26 (48) (2016) 8810–8823, https://doi.org/10.1002/adfm.201603197.
[14] D. Tang, R.S. Tare, L.Y. Yang, D.F. Williams, R.O.C. Oreffo, Biofabrication of bone tissue: approaches, challenges and translation for bone regeneration, Biomaterials 83 (2016) 363–382, https://doi.org/10.1016/j.biomaterials.2016.01.024.
[15] C.B. Fox, J. Kim, E.B. Schlesinger, H.D. Chirra, T.A. Desai, Fabrication of micropatterned polymeric nanowire arrays for high-resolution reagent localization and topographical cellular control, Nano Lett. 15 (3) (2015) 1540–1546, https://doi.org/10.1021/nl503872p.
[16] H. Wu, T. Liu, Z. Xu, J. Qian, X. Shen, Y. Li, Y. Pan, D. Wang, K. Zheng, A. R. Boccaccini, J. Wei, Enhanced bacteriostatic activity, osteogenesis and osseointegration of silicon nitride/polyetherketoneketone composites with femtosecond laser induced micro/nano structural surface, Appl. Mater. Today 18 (2020) 100523, https://doi.org/10.1016/j.apmt.2019.100523.
[17] P. Jiang, J. Liang, R. Song, Y. Zhang, L. Ren, L. Zhang, P. Tang, C. Lin, Effect of octacalcium-phosphate-modified micro/nanostructured titania surfaces on osteoblast response, ACS Appl. Mater. Interfaces 7 (26) (2015) 14384–14396, https://doi.org/10.1021/acsami.5b03172.
[18] C. Yang, C. Zhao, X. Wang, M. Shi, Y. Zhu, L. Jing, C. Wu, J. Chang, Stimulation of osteogenesis and angiogenesis by micro/nano hierarchical hydroxyapatite via macrophage immunomodulation, Nanoscale 11 (38) (2019) 17699–17708, https://doi.org/10.1039/c9nr05730g.
[19] L. Xia, K. Lin, X. Jiang, B. Fang, Y. Xu, J. Liu, D. Zeng, M. Zhang, X. Zhang, J. Chang, Effect of nano-structured bioceramic surface on osteogenic differentiation of adipose derived stem cell, Biomaterials 35 (30) (2014) 8514–8527, https://doi.org/10.1016/j.biomaterials.2014.06.028.
[20] C. Zhao, X. Wang, L. Gao, L. Jing, Q. Zhou, J. Chang, The role of the micro-pattern and nano-topography of hydroxyapatite bioceramics on stimulating osteogenic differentiation of mesenchymal stem cells, Acta Biomater. 73 (2018) 509–521, https://doi.org/10.1016/j.actbio.2018.04.030.
[21] R. Zhao, S. Chen, B. Yuan, X. Chen, X. Yang, Y. Song, H. Tang, X. Yang, X. Zhu, X. Zhang, Healing of osteoporotic bone defects by micro-/nano-structured calcium phosphate bioceramics, Nanoscale 11 (6) (2019) 2721–2732, https://doi.org/10.1039/c8nr09417a.
[22] Y. Zhu, K. Zhang, R. Zhao, X. Ye, X. Chen, Z. Xiao, X. Yang, X. Zhu, K. Zhang, Y. Fan, Bone regeneration with micro/nano hybrid-structured biphasic calcium phosphate bioceramics at segmental bone defect and the induced immunoregulation of MSCs, Biomaterials 147 (2017) 133–144, https://doi.org/10.1016/j.biomaterials.2017.09.018.
[23] Q.Q. Wan, W.P. Qin, M.J. Shen, Y.X. Ma, B. Li, S.Y. Liu, F.R. Tay, K. Jiao, L.N. Niu, Simultaneous regeneration of bone and nerves through materials and architectural design: are we there yet? Adv. Funct. Mater. 30 (48) (2020) 2003542, https://doi.org/10.1002/adfm.202003542.
[24] J. Jin, G. Zuo, G. Xiong, H. Luo, Q. Li, C. Ma, D. Li, F. Gu, Y. Ma, Y. Wan, The inhibition of lamellar hydroxyapatite and lamellar magnetic hydroxyapatite on the migration and adhesion of breast cancer cells, J. Mater. Sci. Mater. Med. 25 (4) (2014) 1025–1031, https://doi.org/10.1007/s10856-013-5126-8.
[25] Z. Li, J. Tang, H. Wu, Z. Ling, S. Chen, Y. Zhou, B. Guo, X. Yang, X. Zhu, L. Wang, C. Tu, X. Zhang, A systematic assessment of hydroxyapatite nanoparticles used in the treatment of melanoma, Nano Res. 13 (8) (2020) 2106–2117, https://doi.org/10.1007/s12274-020-2817-6.
[26] K. Zhang, Y. Zhou, C. Xiao, W. Zhao, H. Wu, J. Tang, Z. Li, S. Yu, X. Li, L. Min, Z. Yu, G. Wang, L. Wang, K. Zhang, X. Yang, X. Zhu, C. Tu, X. Zhang, Application of hydroxyapatite nanoparticles in tumor-associated bone segmental defect, Sci. Adv. 5 (8) (2019), eaax6946, https://doi.org/10.1126/sciadv.aax6946.
[27] R. Zhao, P. Xie, K. Zhang, Z. Tang, X. Chen, X. Zhu, Y. Fan, X. Yang, X. Zhang, Selective effect of hydroxyapatite nanoparticles on osteoporotic and healthy bone formation correlates with intracellular calcium homeostasis regulation, Acta Biomater. 59 (1) (2017) 338–350, https://doi.org/10.1016/j.actbio.2017.07.009.
[28] B. Yuan, L. Wang, R. Zhao, X. Yang, X. Yang, X. Zhu, L. Liu, K. Zhang, Y. Song, X. Zhang, A biomimetically hierarchical polyetherketoneketone scaffold for osteoporotic bone repair, Sci. Adv. 6 (50) (2020), eabc4704, https://doi.org/10.1126/sciadv.abc4704.
[29] C. Zhou, X. Ye, Y. Fan, L. Ma, Y. Tan, F. Qing, X. Zhang, Biomimetic fabrication of a three-level hierarchical calcium phosphate/collagen/hydroxyapatite scaffold for bone tissue engineering, Biofabrication 6 (2014), 035013, https://doi.org/10.1088/1758-5082/6/3/035013.
[30] X. Ye, C. Zhou, Z. Xiao, Y. Fan, X. Zhu, Y. Sun, X. Zhang, Fabrication and characterization of porous 3D whisker-covered calcium phosphate scaffolds, Mater. Lett. 128 (1) (2014) 179–182, https://doi.org/10.1016/j.matlet.2014.04.142.
[31] R. Zhao, S. Chen, W. Zhao, L. Yang, B. Yuan, V.S. Ioan, A.V. Iulian, X. Yang, X. Zhu, X. Zhang, A bioceramic scaffold composed of strontium-doped three-dimensional hydroxyapatite whiskers for enhanced bone regeneration in osteoporotic defects, Theranostics 10 (4) (2020) 1572–1589, https://doi.org/10.7150/thno.40103.
[32] M. Tzaphlidou, V. Zaichick, Sex and age related Ca/P ratio in cortical bone of iliac crest of healthy humans, J. Radioanal. Nucl. Chem. 259 (2) (2004) 347–349, https://doi.org/10.1023/B:JRNC.0000017316.20693.45.
[33] Y. Xiao, H.C. Yong, P. Muthukumaran, S. Dasde, S.H. Teoh, T. Lee, Ibandronate does not reduce the anabolic effects of PTH in ovariectomized rat tibiae: a microarchitectural and mechanical study, Bone 48 (5) (2011) 1154–1163, https://doi.org/10.1016/j.bone.2011.02.007.
[34] J. Huang, H. Yin, S.S. Rao, P.L. Xie, X. Cao, T. Rao, S.Y. Liu, Z.X. Wang, J. Cao, Y. Hu, Harmine enhances type H vessel formation and prevents bone loss in ovariectomized mice, Theranostics 8 (9) (2018) 2435–2446, https://doi.org/10.7150/thno.22144.
[35] A.P. Kusumbe, S.K. Ramasamy, R.H. Adams, Coupling of angiogenesis and osteogenesis by a specific vessel subtype in bone, Nature 507 (7492) (2014) 323–328, https://doi.org/10.1038/nature13145.
[36] Y. Cui, T. Zhu, D. Li, Z. Li, J. Ding, Bisphosphonate-Functionalized scaffolds for enhanced bone regeneration, Adv. Healthc. Mater. 8 (23) (2019) 1901073, https://doi.org/10.1002/adhm.201901073.
[37] E.R. Urquia Edreira, A. Hayrapetyan, J.G. Wolke, H.J. Croes, A. Klymov, J. A. Jansen, V.D.B. Jj, Effect of calcium phosphate ceramic substrate geometry on mesenchymal stromal cell organization and osteogenic differentiation, Biofabrication 8 (2) (2016), 025006, https://doi.org/10.1088/1758-5090/8/2/025006.
[38] A. Xu, X. Liu, X. Gao, F. Deng, Y. Deng, S. Wei, Enhancement of osteogenesis on micro/nano-topographical carbon fiber-reinforced polyetheretherketone-nanohydroxyapatite biocomposite, Mater. Sci. Eng. C Mater. Biol. Appl. 48 (2015) 592–598, https://doi.org/10.1016/j.msec.2014.12.061.
[39] Y. Wang, J. Zhang, C. Jin, X. Chen, Study on the performance of fiber-latex-calcium carbonate whisker gas storage cement, IOP Conf. Ser. Earth Environ. Sci. 558 (3) (2020), https://doi.org/10.1088/1755-1315/558/3/032006, 032006-032009.
[40] K.N. Tu, J.C.M. Li, Spontaneous whisker growth on lead-free solder finishes, Mater. Sci. Eng., A 409 (1/2) (2005) 131–139, https://doi.org/10.1016/j.msea.2005.06.074.
[41] Y. Chen, Z. Sun, Y. Li, Y. Hong, Osteogenic commitment of mesenchymal stem cells in apatite nanorod-aligned ceramics, ACS Appl. Mater. Interfaces 6 (24) (2014) 21886–21893, https://doi.org/10.1021/am5064662.
[42] C. Feng, Y. Wu, Q. Cao, X. Li, X. Zhang, Effect of Hydrothermal Media on the in-situ whisker growth on biphasic calcium phosphate ceramics, Int. J. Nanomed. 16 (2021) 147–159, https://doi.org/10.2147/IJN.S280130.
[43] X.Q. Duan, Y.H. Li, X.Y. Zhang, Z.T. Zhao, Y. Wang, H. Wang, G.S. Li, L. Jing, Mechanisms of intracellular calcium homeostasis in MC3T3-E1 cells and bone tissues of Sprague-Dawley rats exposed to fluoride, Biol. Trace Elem. Res. 170 (2) (2016) 331–339, https://doi.org/10.1007/s12011-015-0465-6.
[44] A. Borsy, J. Podani, V. Stéger, B. Balla, A. Horváth, J.P. Kósa, I. Gyurján Jr., A. Molnár, Z. Szabolcsi, L. Szabó, E. Jakó, Z. Zomborszky, J. Nagy, S. Semsey, T. Vellai, P. Lakatos, L. Orosz, Identifying novel genes involved in both deer physiological and human pathological osteoporosis, Mol. Genet. Genom. 281 (3) (2009) 301–313, https://doi.org/10.1007/s00438-008-0413-7.
[45] M. Zhao, H. Li, X. Liu, J. Wei, J. Ji, S. Yang, Z. Hu, S. Wei, Response of human osteoblast to n-HA/PEEK—quantitative proteomic study of bio-effects of nano-hydroxyapatite composite, Sci. Rep. 6 (2016) 22832, https://doi.org/10.1038/srep22832.
[46] S. Goebel, J. Lienau, U. Rammoser, L. Seefried, K.F. Wintgens, J. Seufert, G. Duda, F. Jakob, R. Ebert, FGF23 is a putative marker for bone healing and regeneration, J. Orthopaed. Res. Off. Publ. Orthopaed. Res. Soc. 27 (9) (2010) 1141–1146, https://doi.org/10.1002/jor.20857.
[47] Y. Sai, Y. Shiwaku, T. Anada, K. Tsuchiya, T. Takahashi, O. Suzuki, Capacity of octacalcium phosphate to promote osteoblastic differentiation toward osteocytes in vitro, Acta Biomater. 69 (2018) 362–371, https://doi.org/10.1016/j.actbio.2018.01.026.
[48] A. Kale, I. Amende, K. Piskorski, V. Chu, J.M. Otero, P. Mueller, T.G. Hampton, Non-invasive physiology in conscious mice, Alternat. Labor. Anim. 32 (1) (2004) 195–201, https://doi.org/10.1177/026119290403201s33.
[49] J. Lu, X. Sun, H. Yin, X. Shen, S. Yang, Y. Wang, W. Jiang, Y. Sun, L. Zhao, X. Sun, S. Lu, A.G. Mikos, J. Peng, X. Wang, A neurotrophic peptide-functionalized self-assembling peptide nanofiber hydrogel enhances rat sciatic nerve regeneration, Nano Res. 11 (9) (2018) 4599–4613, https://doi.org/10.1007/s12274-018-2041-9.
[50] C.H. Wu, Y.F. Chang, C.H. Chen, E.M. Lewiecki, C. Wüster, I. Reid, K.S. Tsai, T. Matsumoto, L.B. Mercado-Asis, D.C. Chan, J.S. Hwang, C.L. Cheung, K. Saag, J. K. Lee, S.T. Tu, W. Xia, W. Yu, Y.S. Chung, P. Ebeling, A. Mithal, S.L. Ferrari, C. Cooper, G.T. Lin, R.S. Yang, Consensus statement on the use of bone turnover markers for short-term monitoring of osteoporosis treatment in the Asia-Pacific region, J. Clin. Densitom. 24 (1) (2019) 3–13, https://doi.org/10.1016/j.jocd.2019.03.004.
[51] S. Ray, U. Thormann, M. Eichelroth, M.U. Budak, C. Biehl, M. Rupp, U. Sommer, T. El Khassawna, F.I. Alagboso, M. Kampschulte, Strontium and bisphosphonate coated iron foam scaffolds for osteoporotic fracture defect healing, Biomaterials 157 (2017) 1–16, https://doi.org/10.1016/j.biomaterials.2017.11.049.
[52] L. Li, M. Yu, Y. Li, Q. Li, H. Yang, M. Zheng, Y. Han, D. Lu, S. Lu, L. Gui, Synergistic anti-inflammatory and osteogenic n-HA/resveratrol/chitosan composite microspheres for osteoporotic bone regeneration, Bioact. Mater. 6 (5) (2021) 1255–1266, https://doi.org/10.1016/j.bioactmat.2020.10.018.
[53] V. Mathieu, R. Vayron, G. Richard, G. Lambert, S. Naili, J.P. Meningaud, G. Haiat, Biomechanical determinants of the stability of dental implants: influence of the bone-implant interface properties, J. Biomech. 47 (1) (2014) 3–13, https://doi.org/10.1016/j.jbiomech.2013.09.021.
[54] C. McManamon, J.P. de Silva, J. Power, S. Ramirez-Garcia, M.A. Morris, G.L. W. Cross, Interfacial characteristics and determination of cohesive and adhesive strength of plasma-coated hydroxyapatite via nanoindentation and microscratch

techniques, Langmuir 30 (38) (2014) 11412–11420, https://doi.org/10.1021/la502802f.
[55] X. Yang, P. Muthukumaran, S. Dasde, S.H. Teoh, H. Choi, S.K. Lim, T. Lee, Positive alterations of viscoelastic and geometric properties in ovariectomized rat femurs with concurrent administration of ibandronate and PTH, Bone 52 (1) (2013) 308–317, https://doi.org/10.1016/j.bone.2012.09.039.
[56] L.J. Jiao, A. Austin, C.R. Dunstan, V. Martin, F. Oliver, D.C. Bell, Z. Hala, Effects of material-tissue interactions on bone regeneration outcomes using baghdadite implants in a large animal model, Adv. Healthc. Mater. 7 (15) (2018), e1800218, https://doi.org/10.1002/adhm.201800218.
[57] S. Chen, R. Zhao, Z. Xing, T. Shang, X. Zhang, Strontium combined with bioceramics for osteoporotic bone repair: oral intake or as a dopant? Appl. Mater. Today 22 (2021) 100927, https://doi.org/10.1016/j.apmt.2020.100927.
[58] Z. Tang, X. Li, Y. Tan, H. Fan, X. Zhang, The material and biological characteristics of osteoinductive calcium phosphate ceramics, Regen. Biomater. 5 (1) (2017) 43–59, https://doi.org/10.1093/rb/rbx024.
[59] B.S. Chang, C.K. Lee, K.S. Hong, H.J. Youn, H.S. Ryu, S.S. Chung, K.W. Park, Osteoconduction at porous hydroxyapatite with various pore configurations, Biomaterials 21 (12) (2000) 1291–1298, https://doi.org/10.1016/s0142-9612(00)00030-2.
[60] Y. Zhao, K. Tan, Y. Zhou, Z. Ye, W.S. Tan, A combinatorial variation in surface chemistry and pore size of three-dimensional porous poly(ε-caprolactone) scaffolds modulates the behaviors of mesenchymal stem cells, Mater. Sci. Eng. C Mater. Biol. Appl. 59 (2016) 193–202, https://doi.org/10.1016/j.msec.2015.10.017.